The Astronomical Journal, 160:277 (14pp), 2020 December https://doi.org/10.3847/1538-3881/abc3bc

Establishing Earth's Minimoon Population through Characterization of Asteroid 2020 CD_3

Grigori Fedorets[1], Marco Micheli[2,3], Robert Jedicke[4], Shantanu P. Naidu[5], Davide Farnocchia[5], Mikael Granvik[6,7], Nicholas Moskovitz[8], Megan E. Schwamb[1], Robert Weryk[4], Kacper Wierzchoś[9], Eric Christensen[9], Theodore Pruyne[9], William F. Bottke[10], Quanzhi Ye[11], Richard Wainscoat[4], Maxime Devogèle[8,12], Laura E. Buchanan[1], Anlaug Amanda Djupvik[13], Daniel M. Faes[14], Dora Föhring[4], Joel Roediger[15], Tom Seccull[14], and Adam B. Smith[14]
[1] Astrophysics Research Centre, School of Mathematics and Physics, Queen's University Belfast, Belfast BT7 1NN, UK; fedorets@iki.fi
[2] ESA NEO Coordination Centre, Largo Galileo Galilei, 1, I-00044 Frascati (RM), Italy
[3] INAF—Osservatorio Astronomico di Roma, Via Frascati, 33, I-00040 Monte Porzio Catone (RM), Italy
[4] University of Hawai'i, Institute for Astronomy, 2680 Woodlawn Drive, Honolulu, HI 96822, USA
[5] Jet Propulsion Laboratory, California Institute of Technology, Pasadena, CA 91109, USA
[6] Department of Physics, P.O. Box 64, FI-00014, University of Helsinki, Finland
[7] Asteroid Engineering Laboratory, Onboard Space Systems, Luleå University of Technology, Box 848, SE-98128 Kiruna, Sweden
[8] Lowell Observatory, 1400 W Mars Hill Road, Flagstaff, AZ 86001, USA
[9] The University of Arizona, Lunar and Planetary Laboratory, 1629 E. University Boulevard, Tucson, AZ 85721, USA
[10] Department of Space Studies, Southwest Research Institute, 1050 Walnut Street, Suite 300, Boulder, CO 80302, USA
[11] Department of Astronomy, University of Maryland, College Park, MD 20742, USA
[12] Arecibo Observatory, University of Central Florida, HC-3 Box 53995, Arecibo, PR 00612, USA
[13] Nordic Optical Telescope, Apartado 474, E-38700 Santa Cruz de La Palma, Santa Cruz de Tenerife, Spain
[14] Gemini Observatory/NSF's NOIRLab, 670 N. A'ohoku Place, Hilo, HI 96720, USA
[15] National Research Council of Canada, Herzberg Astronomy and Astrophysics Research Centre, 5071 West Saanich Road, Victoria, BC V9E 2E7, Canada
Received 2020 August 11; revised 2020 October 20; accepted 2020 October 20; published 2020 November 23

Abstract

We report on our detailed characterization of Earth's second known temporary natural satellite, or minimoon, asteroid 2020 CD_3. An artificial origin can be ruled out based on its area-to-mass ratio and broadband photometry, which suggest that it is a silicate asteroid belonging to the S or V complex in asteroid taxonomy. The discovery of 2020 CD_3 allows for the first time a comparison between known minimoons and theoretical models of their expected physical and dynamical properties. The estimated diameter of $1.2^{+0.4}_{-0.2}$ m and geocentric capture approximately a decade after the first known minimoon, 2006 RH_{120}, are in agreement with theoretical predictions. The capture duration of 2020 CD_3 of at least 2.7 yr is unexpectedly long compared to the simulation average, but it is in agreement with simulated minimoons that have close lunar encounters, providing additional support for the orbital models. 2020 CD_3's atypical rotation period, significantly longer than theoretical predictions, suggests that our understanding of meter-scale asteroids needs revision. More discoveries and a detailed characterization of the population can be expected with the forthcoming Vera C. Rubin Observatory Legacy Survey of Space and Time.

Unified Astronomy Thesaurus concepts: Near-Earth objects (1092); Asteroids (72); Transient sources (1851); Astrometry (80); Broad band photometry (184); Earth-moon system (436); Light curves (918); Orbit determination (1175)

1. Introduction

Asteroids and comets can be temporarily captured by planets as natural satellites. Theoretical models (Granvik et al. 2012; Fedorets et al. 2017) predict that Earth is also surrounded by a cloud of such temporarily captured asteroids, colloquially called minimoons. The largest minimoon captured at any given time is 1 m in diameter, while larger bodies are captured less frequently.

Minimoons possess a number of attributes that make them objects of particular interest. As they spend an extended amount of time in the vicinity of Earth, they can provide several windows of opportunity to obtain observations of the little-studied population of meter-class asteroids. The systematic discovery and population statistics of meter- to decameter-class minimoons, a subpopulation of near-Earth objects (NEOs), could resolve existing disagreements between extrapolations of different NEO size–frequency distribution models to this size range—i.e., those based on telescopic observations (e.g., Rabinowitz et al. 2000; Harris & D'Abramo 2015; Granvik et al. 2016; Tricarico 2017) and those based on bolide data (Brown et al. 2002, 2013). Also, due to their relatively long capture duration, accessibility, and small size, minimoons are viable targets for taking the first practical steps in the emerging field of asteroid in situ resource utilization (Granvik et al. 2013; Jedicke et al. 2018a). So far, the primary obstacle for organizing their study has been a lack of observational evidence supporting the existence of a minimoon population to the extent predicted by the models.

Up until 2020, only one minimoon (2006 RH_{120}; Bressi et al. 2008; Kwiatkowski et al. 2009) had been discovered. The second known minimoon, 2020 CD_3, was discovered on 2020 February 15.51 UT by the Catalina Sky Survey (CSS; Christensen et al. 2018) 1.5 m telescope on Mt. Lemmon (Minor Planet Center 2020). One day later, an alert automatically sent out by the NASA Jet Propulsion Laboratory's Scout system (Farnocchia et al. 2015a, 2016) announced that it was likely temporarily captured in the Earth–Moon system. Discovering an object on a geocentric orbit always raises suspicion of an artificial origin, but during the 2.5 weeks following its discovery, 2020 CD_3 could not be linked to any known artificial object nor could a natural origin be ruled out.

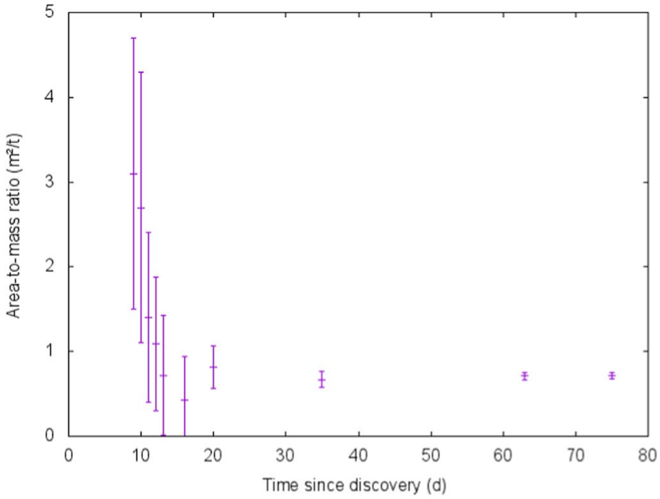

Figure 1. The evolution of the detection of the zero-albedo area-to-mass ratio with 1σ error bars as a function of the length of the observational arc.

On 2020 February 26, the Minor Planet Center (MPC) therefore added 2020 CD$_3$ to the catalog of asteroids as a temporarily captured object with a request for further follow-up observations to establish its nature (Minor Planet Center 2020).

The nominal solution for the area-to-mass ratio of 2020 CD$_3$—calculated from the solar radiation pressure signature on the orbital solution, and a diagnostic quantity for distinguishing between natural and artificial objects (Jedicke et al. 2018a)—decreased during the two weeks after discovery (Figure 1), indicating that it might be a natural object. To characterize the potential minimoon, we obtained high-precision astrometric follow-up observations in 2020 February–May with the Nordic Optical Telescope (NOT), Canada–France–Hawai'i Telescope (CFHT), Lowell Discovery Telescope (LDT), University of Hawai'i 2.2 m telescope (UH 2.2), and the Calar Alto Schmidt telescope; broadband photometric observations from Gemini North; and rotational lightcurve observations with LDT. In addition, a search for prediscovery detections with the Pan-STARRS surveys (Chambers et al. 2016), Zwicky Transient Facility (Bellm et al. 2019; Masci et al. 2019), Catalina Sky Survey (Christensen et al. 2018), and Chinese Near-Earth Object Survey Telescope (Zhao et al. 2007) was performed.

In this work, we provide a detailed characterization of the physical properties and orbital evolution of 2020 CD$_3$. We also discuss its detectability and assess the possibility of its lunar origin. We describe the observations and precovery attempts in detail in Section 2 outline the data reduction and methods for physical characterization and orbit computation in Section 3, present the results and discuss the implications in Section 4, and offer our conclusions in Section 5.

2. Data Acquisition

2.1. Instruments and Observations

An overview of all instruments used in this analysis is provided in Table 1. 2020 CD$_3$ was discovered on 2020 February 15.51 UT by the Catalina Sky Survey (CSS; Christensen et al. 2018) 1.5 m telescope on Mt. Lemmon (MPC observatory code G96). Upon discovery, the object was favorably placed near the ecliptic plane $\sim$45° east of opposition. The discovery image sequence consisted of four 30 s exposures, with $\sim$7 minute separation between each successive image, that were inspected soon after the final image by two observers and submitted to the MPC as a new NEO candidate. After the object was placed on the MPC's NEO Confirmation Page, additional same-night follow-up observations were performed with the same telescope that was used to discover 2020 CD$_3$.

Multiple broadband photometric imaging was performed on 2020 February 24 with the 8.1 m Frederick C. Gillett Gemini North Telescope located on Maunakea, Hawaiʻi, USA. The Gemini Multi-Object Spectrograph (GMOS; Hook et al. 2004) observations consisted of three $r'g'i'$ sequences with the G0301, G0303, and G0302 filters, taken in photometric conditions with Image Quality 85 ($1\overset{\prime\prime}{.}05$ full zenith corrected seeing) or better seeing. The telescope was tracked nonsidereally at 2020 CD$_3$'s rate of motion, thereby maintaining its stellar point-spread function (PSF) for photometry but elongating the reference field stars. We also obtained sidereally tracked images in the three filters immediately before and after the nonsidereal tracking of 2020 CD$_3$ in order to perform absolute photometry.

To obtain 2020 CD$_3$'s photometric lightcurve, we employed the Large Monolithic Imager (LMI) on the 4.3 m Lowell Discovery Telescope (LDT, G37) for approximately 1 hr on 2020 February 27 UTC. Exposures were taken with 30 s integrations using a broadband *VR* filter that provides high throughput between approximately 500 and 700 nm. LMI was binned 3×3 for an effective plate scale of $0\overset{\prime\prime}{.}36$ pixel^{-1} and the telescope was tracked at the nonsidereal rates of the target. On several later occasions, we used LDT/LMI to obtain astrometry with a similar technique but without any filters.

The 3.6 m Canada–France–Hawaii Telescope (CFHT, 568) on Maunakea, Hawaiʻi, USA, was used to obtain astrometry using nonsidereal tracking with exposures of up to 120 s in *gri*-band MegaCam images with no pixel binning. MegaCam has $0\overset{\prime\prime}{.}187$ pixels allowing for precise astrometric measurements under good seeing conditions.

Astrometric observations were also made with the Alhambra Faint Object Spectrograph and Camera (ALFOSC) at the 2.5 m Nordic Optical Telescope (NOT, Z23) at the Roque de los Muchachos Observatory, La Palma, Canary islands, Spain. The exposures were tracked nonsidereally on 2020 CD$_3$. Each image's exposure time was set equal to the time it would take for 2020 CD$_3$ to move at most one stellar FWHM on the sky. Most of the 2020 CD$_3$ detections had signal-to-noise ratio (S/N) $\geqslant$ 15, but the last observations reached only S/N $\sim$ 5 as the target reached the detection threshold. The observations were performed without any filters with 4×4 pixel binning.

The University of Hawaii 2.2 m (UH 2.2, 568) telescope was used for astrometric observations with nonsidereal tracking at 2020 CD$_3$'s apparent rates of motion in unfiltered 300 s exposures. Additional astrometric observations were extracted from dedicated early observations obtained with the Calar Alto Schmidt telescope (Z84) in Spain. The detections were obtained from a set of short sidereally tracked frames, stacked with respect to the known motion of the object.

2.2. Search for Prediscovery Detections

The image archives for several survey telescopes were searched for prediscovery observations of 2020 CD$_3$ by generating an ephemeris for each exposure and visually examining any potential matches. The 1.8 m Pan-STARRS1 telescope (F51) has an extensive archive dating back to 2010

Table 1
Telescopes Used in This Work and Their Purpose

Telescope	Aperture (m)	Astrometry	Photometry	Lightcurve
CSS Mt. Lemmon	1.5	✓		
Calar Alto Schmidt	0.8	✓		
Nordic Optical Telescope	2.5	✓		
Gemini North	8.1		✓	
Canada–France–Hawai'i Telescope	3.6	✓		
Lowell Discovery Telescope	4.3	✓		✓
U. of Hawai'i 2.2 m	2.2	✓		

(Chambers et al. 2016) and is sensitive to $V \sim 23$, but no detections were found. The Zwicky Transient Facility (ZTF, I41) is an ongoing wide-field optical survey using the 1.2 m Palomar Oschin Schmidt telescope and has been in operation since 2018 (Bellm et al. 2019; Graham et al. 2019; Masci et al. 2019). No detections were found in its Data Release 3 (DR3) archive that extends from 2018 March to the end of 2019 December. The Chinese NEO Survey Telescope (CNEOST, D29; Zhao et al. 2007) is a 1.0 m Schmidt telescope at Xuyi, Jiangsu, China, equipped with a $3^\circ \times 3^\circ$ camera. We searched images taken between 2018 January and 2019 May (when the telescope went offline for hardware upgrades) but did not find any matching fields. Lastly, we checked all of the telescopes used by the Catalina Sky Survey for prediscovery opportunities and found only two suitable fields imaged by the Mt. Lemmon telescope (G96) on 2019 November 9 and 2019 January 24, close to times when the object was expected to be at perigee and therefore relatively bright. Significant trailing losses, the spreading of the light from the target over many pixels due to its motion during an exposure, combined with nonoptimal sky conditions, prevented a detection in both images. In summary, the signals in the possible images were mostly smeared by trailing losses, and no detections were found from any of the mentioned surveys.

3. Data Reduction and Calculations

3.1. Astrometric Data Reduction

Due to the different observing strategies and capabilities of each instrument/telescope combination, each image set was astrometrically analyzed with different techniques. In some cases, a direct measurement on individual frames was possible by fitting 2020 CD_3's detection to a stellar PSF or trail. In other cases, especially later in the apparition, we stacked multiple frames at 2020 CD_3's (often rapidly changing) rates of motion to achieve sufficient S/N for a measurable detection. We carefully estimated our formal astrometric uncertainty by taking into account contributions from the object's S/N (often dominant) and also from the astrometric solution, now typically negligible thanks to the Gaia DR2 catalog (Gaia Collaboration et al. 2016, 2018; Lindegren et al. 2018), to which all the astrometry was calibrated. For all instruments used in the analysis, an assessment of the timing accuracy was also included. In most cases, a conservative timing uncertainty of 1 s was assumed. When timing biases were suspected, we only included the cross-track component of the astrometric position in the astrometric fit and deweighted the along-track direction. All acquired and remeasured astrometry is provided in Table 2.

The peculiarities of 2020 CD_3's outgoing trajectory and, in particular, its low relative velocity with respect to Earth, kept the object at small geocentric distances for many weeks after discovery. As a result, most of the astrometric coverage was obtained when topocentric parallax was significant, and it is essential to know the precise and accurate location of the observing telescope, ideally to within a few meters in the Gaia catalog era. We therefore dedicated significant effort to obtain accurate coordinates and/or codes for all telescopes we used to extract observations of 2020 CD_3.

3.2. Photometric Data Reduction

The raw GMOS-N data frames were reduced using standard techniques with the Gemini DRAGONS Python package (Data Reduction for Astronomy from Gemini Observatory North and South, AURA Gemini Observatory-Science User Support Department 2018). Nightly bias frames and twilight flats from the several nights surrounding the observations were used to create the master bias and flat fields. The DAOPHOT software package (Stetson 1987), embedded in the Image Reduction and Analysis Facility (IRAF; Tody 1986, 1993), was used to perform aperture photometry for all GMOS images. The photometry was calibrated to the Sloan Digital Sky Survey (SDSS) photometric system (g', r', and i', Fukugita et al. 1996) with the SDSS Data Release catalog 12 (Alam et al. 2015), accessed through the SkyServer platform. The resulting individual measurements and errors of GMOS photometry are provided in Table 3. The resulting magnitudes in each filter are mean values of individual measurements with respective filters. That way we diminish the effect of the brightness variations induced by the rotation of the asteroid.

The set of images obtained with LDT/LMI for the lightcurve were reduced using standard bias subtraction and flat-field correction from facility dome flats. 2020 CD_3's photometry was measured using the Photometry Pipeline (Mommert 2017). This pipeline extracted sources with SourceExtractor using a 3 pixel ($1\farcs08$) aperture (Bertin & Arnouts 1996), astrometrically registered the images based on the Gaia DR2 catalog (Gaia Collaboration et al. 2018), and then determined the zero-point calibration for each image by referencing to approximately 50 field stars from the Pan-STARRS DR1 catalog (Flewelling et al. 2020). The photometric calibration was performed by tying the *VR* images to the Pan-STARRS1 $r_{\rm P1}$ band. This technique introduces errors in the absolute photometric calibration as the bands are not identical but they are significantly smaller than the typical uncertainty (∼0.1–0.2 mag) on the individual measurements. All data points for the lightcurve are provided in Table 4.

3.3. Calculations of Area-to-mass Ratio, Albedo, Density, and Phase Curve

The astrometric data show that the motion of 2020 CD_3 is significantly affected by solar radiation pressure. Establishing

Table 2
Newly Acquired or Remeasured Astrometric Data for 2020 CD_3

Date (UTC)	α	δ	G	Code	σ_α	σ_δ	Telescope
2020 02 15.526427	13 03 37.570	+09 17 38.40	19.6	G96	0.11	0.16	CSS Mt. Lemmon
2020 02 17.975500	13 45 24.910	+19 18 44.71	21.0	Z84	0.30	0.30	Calar Alto Schmidt
2020 02 17.984601	13 45 26.960	+19 20 34.07	20.9	Z84	0.32	0.32	Calar Alto Schmidt
2020 02 17.993701	13 45 28.601	+19 22 22.81	21.1	Z84	0.21	0.21	Calar Alto Schmidt
2020 02 18.002805	13 45 29.872	+19 24 10.44	21.0	Z84	0.22	0.22	Calar Alto Schmidt
2020 02 18.011907	13 45 30.718	+19 25 57.10	21.3	Z84	0.17	0.17	Calar Alto Schmidt
2020 02 18.021008	13 45 31.196	+19 27 42.04	21.3	Z84	0.19	0.19	Calar Alto Schmidt
2020 02 21.093805	14 03 50.575	+24 20 51.66	21.8	Z84	0.24	0.24	Calar Alto Schmidt
2020 02 21.114761	14 03 44.360	+24 22 47.25	21.8	Z84	0.27	0.27	Calar Alto Schmidt
2020 02 21.177717	14 03 22.794	+24 27 37.51	21.8	Z84	0.23	0.23	Calar Alto Schmidt
2020 02 21.198677	14 03 15.400	+24 28 53.86	21.7	Z84	0.15	0.15	Calar Alto Schmidt
2020 02 21.174711	14 03 52.507	+24 31 07.79	22.0	Z23	0.13	0.15	NOT
2020 02 21.199832	14 03 42.272	+24 33 04.85	21.6	Z23	0.10	0.12	NOT
2020 02 21.203876	14 03 40.597	+24 33 22.12	21.6	Z23	0.07	0.07	NOT
2020 02 24.586055	14 14 38.369	+27 28 39.86	22.6	568	0.038	0.036	Gemini North
2020 02 24.601986	14 14 31.235	+27 29 19.63	22.9	568	0.053	0.054	Gemini North
2020 02 24.608418	14 14 28.325	+27 29 34.13	22.8	568	0.034	0.033	Gemini North
2020 02 24.621399	14 14 22.582	+27 30 00.12	22.4	568	0.107	0.041	Gemini North
2020 02 25.148888	14 16 23.887	+27 46 14.71	23.6	Z23	0.2	0.2	NOT
2020 02 25.156760	14 16 21.045	+27 46 42.49	22.7	Z23	0.08	0.08	NOT
2020 02 25.161406	14 16 19.302	+27 46 58.27	22.7	Z23	0.11	0.11	NOT
2020 02 26.608875	14 18 35.299	+28 40 16.90	23.0	568	0.047	0.041	UH 2.2 m
2020 02 26.613020	14 18 33.500	+28 40 23.38	23.0	568	0.060	0.049	UH 2.2 m
2020 02 26.616949	14 18 31.802	+28 40 29.28	23.2	568	0.075	0.078	UH 2.2 m
2020 02 26.620998	14 18 30.056	+28 40 34.90	23.2	568	0.057	0.049	UH 2.2 m
2020 02 26.625629	14 18 28.070	+28 40 40.98	23.0	568	0.055	0.045	UH 2.2 m
2020 02 26.620384	14 18 30.334	+28 40 34.01	22.76	568	0.05	0.05	CFHT
2020 02 26.621564	14 18 29.827	+28 40 35.61	22.77	568	0.05	0.05	CFHT
2020 02 26.622763	14 18 29.317	+28 40 37.19	22.74	568	0.05	0.05	CFHT
2020 02 28.594550	14 21 41.875	+29 36 30.86	22.77	568	0.05	0.05	CFHT
2020 02 28.595729	14 21 41.374	+29 36 32.58	23.19	568	0.05	0.05	CFHT
2020 02 28.598103	14 21 40.361	+29 36 36.06	23.23	568	0.05	0.05	CFHT
2020 03 01.477536	14 23 44.902	+30 15 25.54	22.6	G37	0.256	0.268	LDT
2020 03 01.479237	14 23 44.291	+30 15 27.50	23.0	G37	0.313	0.283	LDT
2020 03 01.480279	14 23 43.932	+30 15 28.52	22.8	G37	0.213	0.262	LDT
2020 03 02.162378	14 24 45.080	+30 30 46.94	23.2	Z23	0.07	0.07	NOT
2020 03 02.179266	14 24 38.827	+30 31 16.90	23.1	Z23	0.09	0.09	NOT
2020 03 02.655003	14 24 20.964	+30 42 13.62	23.32	568	0.05	0.05	CFHT
2020 03 02.656878	14 24 20.269	+30 42 13.26	23.08	568	0.05	0.05	CFHT
2020 03 02.658754	14 24 19.596	+30 42 12.91	23.13	568	0.05	0.05	CFHT
2020 03 04.635008	14 25 48.907	+31 15 21.90	23.30	568	0.05	0.05	CFHT
2020 03 04.636888	14 25 48.213	+31 15 21.78	23.28	568	0.05	0.05	CFHT
2020 03 04.638761	14 25 47.512	+31 15 21.58	23.28	568	0.05	0.05	CFHT
2020 03 05.489286	14 26 26.653	+31 23 51.85	23.1	G37	0.06	0.06	LDT
2020 03 05.490947	14 26 26.093	+31 23 52.37	22.9	G37	0.06	0.06	LDT
2020 03 05.492737	14 26 25.495	+31 23 52.87	22.9	G37	0.05	0.05	LDT
2020 03 06.240152	14 26 41.654	+31 35 09.84	23.3	Z23	0.06	0.06	NOT
2020 03 06.246311	14 26 39.515	+31 35 09.81	23.7	Z23	0.07	0.07	NOT
2020 03 06.252078	14 26 37.524	+31 35 09.36	23.6	Z23	0.06	0.06	NOT
2020 03 21.462672	14 22 58.469	+33 15 41.15	23.77	568	0.05	0.05	CFHT
2020 03 21.464548	14 22 57.785	+33 15 43.12	23.72	568	0.05	0.05	CFHT
2020 03 21.466429	14 22 57.087	+33 15 45.00	23.59	568	0.05	0.05	CFHT
2020 03 25.199063	14 17 34.589	+33 09 50.72	24.0	Z23	0.12	0.12	NOT
2020 03 25.210295	14 17 30.563	+33 09 39.14	24.2	Z23	0.26	0.26	NOT
2020 03 25.219775	14 17 27.296	+33 09 28.11	23.8	Z23	0.10	0.10	NOT
2020 03 29.161561	14 11 40.795	+32 46 19.67	23.9	Z23	0.08	0.05	NOT
2020 03 29.171345	14 11 37.179	+32 46 09.34	24.1	Z23	0.09	0.06	NOT
2020 03 29.182286	14 11 33.175	+32 45 56.44	24.0	Z23	0.09	0.06	NOT
2020 03 30.376555	14 09 54.750	+32 33 45.95	23.4	G37	0.09	0.08	LDT
2020 03 30.379675	14 09 53.606	+32 33 43.93	23.5	G37	0.17	0.17	LDT
2020 04 17.072836	13 41 35.761	+26 34 34.21	24.1	Z23	0.089	0.102	NOT
2020 04 17.083259	13 41 32.407	+26 34 13.83	24.3	Z23	0.070	0.064	NOT
2020 04 17.093646	13 41 29.074	+26 33 52.11	23.8	Z23	0.207	0.207	NOT
2020 04 29.105118	13 25 42.426	+19 33 24.57		Z23	0.25	0.25	NOT

Table 2
(Continued)

Date (UTC)	α	δ	G	Code	σ_α	σ_δ	Telescope
2020 04 29.113261	13 25 40.749	+19 33 00.44	24.3	Z23	0.25	0.25	NOT
2020 05 15.936339	13 21 25.566	+07 39 09.07	25.0	Z23	0.15	0.15	NOT
2020 05 17.244907	13 21 56.056	+06 44 12.63	24.5	568	0.197	0.152	CFHT
2020 05 17.247704	13 21 55.726	+06 44 05.99	24.3	568	0.281	0.272	CFHT
2020 05 20.950021	13 23 11.161	+04 06 13.56	25.6	Z23	0.10	0.10	NOT
2020 05 20.967845	13 23 09.104	+04 05 28.13	25.4	Z23	0.10	0.10	NOT
2020 05 20.985665	13 23 07.102	+04 04 42.33	25.4	Z23	0.10	0.10	NOT

Note. The columns are, in order from left to right: observation date (UTC); R.A.; decl.; Gaia system magnitude (Jordi et al. 2010); MPC observatory code; R.A. uncertainty in arcseconds; decl. uncertainty in arcseconds; telescope name.

Table 3
Gemini North Photometry of 2020 CD_3

Obs. id	Filter	Mag.	σ_{INST}	σ_{ZP}
1	r'	22.399	0.037	0.048
2	i'	22.269	0.039	0.054
3	r'	22.413	0.035	0.048
4	g'	23.111	0.049	0.033
5	i'	22.267	0.050	0.054
6	r'	22.389	0.040	0.048
7	g'	23.265	0.056	0.033
8	i'	22.340	0.053	0.054

Note. The columns are, from left to right: sequential number of observation; filter; derived magnitude; instrumental error; zero-point error.

its signature with a 3σ detection in about three weeks is two to three times faster than similar analyses in the past. The evolution of the development of the radiation pressure as a function of time is presented in Figure 1. This improvement is due to the enhanced precision and accuracy of the astrometry enabled by the Gaia DR2 catalog (Gaia Collaboration et al. 2018; Lindegren et al. 2018), which permits measuring individual ground-based positions with $0\rlap{.}''05$ accuracy.

In what follows, we interpret the nongravitational acceleration as a result of solar radiation pressure. Following Farnocchia et al. (2015b), we modeled solar radiation pressure perturbation as a purely radial acceleration A_1/r^2, where r is the heliocentric distance. The off-radial components, A_2 and A_3, of the Marsden nongravitational force model (Marsden 1969; Marsden et al. 1973) do not play a significant role in the albedo-density modeling, unlike for the orbital evolution. The A_1 parameter is proportional to the area-to-mass ratio A/m and therefore can provide useful constraints on the physical properties of the object and discern between a natural and artificial origin. For a spherical object,

$$A_1 = A/m\left(1 + \frac{4}{9}A\right)\frac{G_S}{c}\ ,\ A/m = \frac{3}{2D\rho}, \tag{1}$$

where A is the Bond albedo, G_S is the solar constant, c is the speed of light, D the effective diameter, and ρ the density (Vokrouhlický & Milani 2000; Mommert et al. 2014b). We note that this formulation does not take into account the Yarkovsky effect (see Vokrouhlický 1998), which could contribute to 10%–20% of the total radial nongravitational acceleration (e.g., Chesley et al. 2014). Therefore, our calculation is an upper bound estimate of A/m.

The effective diameter D, absolute magnitude H, and geometric albedo p are related as (Pravec & Harris 2007)

$$D = 1329\ \mathrm{km}\frac{10^{-0.2H}}{\sqrt{p}},$$

while the Bond albedo A is the product of the geometric albedo p and the phase integral q,

$$A = p\,q = p\,(0.009082 + 0.4061G_1 + 0.8092G_2),$$

where we have expressed the phase integral q in terms of the G_1, and G_2 photometric parameters (Muinonen et al. 2010).

3.4. Orbit Computation

We used a Monte Carlo approach to analyze 2020 CD_3's past trajectory. We generated 1000 synthetic sets of orbital elements and area-to-mass ratios by sampling the uncertainty region as calculated from the fit to the astrometry. We modeled the solar radiation perturbation using all three coefficients (A_1, A_2, A_3) of the Marsden nongravitational model (Marsden 1969; Marsden et al. 1973). Given the size of 2020 CD_3 and its unknown shape, unlike for the calculation of the area-to-mass ratio, for orbit computation the off-radial components of the solar radiation pressure signature are significant on the timescale of the capture duration. We integrated each synthetic object backwards from 2020 until the object had been captured into the Earth–Moon system. The date of the first perigee within 1 lunar distance (LD) after the insertion into the Earth–Moon system is used as a proxy for the capture date.

Several synthetic objects's orbits were consistent with a lunar origin and their distribution at launch from the Moon's surface is provided in the Appendix assuming that the Moon is a sphere of radius 1737 km. In order to trace the possible origin of 2020 CD_3 from the Moon, we mapped the outbound trajectories of the samples originating from the Moon on the lunar surface. We computed the state vectors of the samples when leaving the Moon's surface and transformed them into the lunar mean Earth/polar axis body-fixed frame (Seidelmann et al. 2002) using NASA's Navigation and Ancillary Information Facility (NAIF) SPICE tools (Acton 1996; Acton et al. 2018).

4. Results and Discussion

4.1. Physical Characterization

We used astrometric observations obtained during the apparition to clearly detect solar radiation pressure acting on 2020 CD_3 and measure its area-to-mass ratio, $A/m = (0.65 \pm 0.05) \times 10^{-3}\ \mathrm{m^2\ kg^{-1}}$. This value implies a natural origin for 2020 CD_3

Table 4
Lightcurve Photometric Data for 2020 CD_3 Obtained with the LDT Translated to the r_{P1} Filter

Date (MJD)	Mag(r_{P1})	σ_{ZP}	σ_{INST}
58906.4881610	22.7116	0.0228	0.1087
58906.4889677	22.6461	0.0215	0.1050
58906.4894715	22.8355	0.0224	0.1289
58906.4899752	22.6235	0.0227	0.1126
58906.4905406	22.9247	0.0216	0.1407
58906.4910444	22.8095	0.0227	0.1270
58906.4915481	23.0082	0.0226	0.1508
58906.4923176	22.8036	0.0218	0.1241
58906.4928214	22.9557	0.0227	0.1618
58906.4933251	22.6341	0.0213	0.1121
58906.4938292	23.1323	0.0232	0.1768
58906.4943329	22.8583	0.0225	0.1346
58906.4953404	22.7895	0.0231	0.1333
58906.4963479	22.8472	0.0229	0.1373
58906.4968516	23.1161	0.0243	0.1807
58906.4973554	23.1744	0.0229	0.1949
58906.5013856	22.9624	0.0229	0.1503
58906.5018894	22.9546	0.0232	0.1508
58906.5029427	22.8884	0.0239	0.1488
58906.5034464	22.6851	0.0234	0.1236
58906.5039502	22.9444	0.0226	0.1473
58906.5049578	23.1792	0.0225	0.1871
58906.5054615	23.0686	0.0220	0.1513
58906.5059652	22.9580	0.0224	0.1486
58906.5074792	22.7658	0.0227	0.1207
58906.5079829	22.9301	0.0223	0.1403
58906.5089904	22.9475	0.0224	0.1535
58906.5094942	22.6765	0.0228	0.1160
58906.5099979	22.8687	0.0225	0.1325
58906.5105017	23.0201	0.0225	0.1490
58906.5110060	22.6124	0.0221	0.1041
58906.5120135	22.6595	0.0231	0.1040
58906.5126895	23.1251	0.0223	0.1675
58906.5131933	22.6779	0.0220	0.1112
58906.5136970	22.9829	0.0231	0.1546
58906.5142007	22.6173	0.0221	0.1030
58906.5147052	22.9908	0.0232	0.1551
58906.5152090	22.6400	0.0225	0.1069
58906.5157131	23.0546	0.0228	0.1527
58906.5162168	22.6199	0.0219	0.1141
58906.5167207	22.6704	0.0226	0.1151
58906.5172244	23.1026	0.0226	0.1690
58906.5177281	22.6366	0.0217	0.1102
58906.5182319	22.8375	0.0225	0.1326
58906.5187356	22.8540	0.0232	0.1375
58906.5192395	22.8399	0.0220	0.1317
58906.5197432	22.6965	0.0221	0.1144
58906.5202471	23.0981	0.0220	0.1653
58906.5207509	22.7457	0.0214	0.1193
58906.5212546	22.8318	0.0218	0.1292
58906.5217587	23.0903	0.0221	0.1685
58906.5222624	22.7996	0.0216	0.1359
58906.5228400	22.6896	0.0227	0.1138
58906.5233449	22.9262	0.0230	0.1470
58906.5238487	23.1095	0.0217	0.1704
58906.5243527	22.7774	0.0224	0.1202
58906.5248564	22.7482	0.0228	0.1234
58906.5253602	22.7669	0.0222	0.1259
58906.5258639	22.9694	0.0228	0.1472
58906.5263677	22.7342	0.0225	0.1164
58906.5283826	23.1254	0.0226	0.1831
58906.5288865	22.8278	0.0224	0.1341
58906.5293902	22.7815	0.0221	0.1421
58906.5298940	22.7310	0.0239	0.1272
58906.5319088	22.7927	0.0230	0.1459

Note. The columns are, from left to right: observation date; measured magnitude; zero-point error; instrumental error.

because it is consistent with A/m for other natural objects in the same size range (Micheli et al. 2012, 2013, 2014; Mommert et al. 2014a, 2014b; Farnocchia et al. 2017) and much lower than typical for artificial objects (Jenniskens et al. 2016).

The derived photometric colors ($g' - r' = 0.8 \pm 0.1$, $r' - i' = 0.15 \pm 0.05$) support 2020 CD_3's natural origin as we do not detect extreme reddening, which is associated with artificial objects (Miles 2011). Our broadband photometry suggests that 2020 CD_3 belongs to the group of silicate asteroids (Figure 2(a)), i.e., to the S or V complexes in the asteroid taxonomy (DeMeo & Carry 2013). Based on physical characterization alone, we cannot exclude that 2020 CD_3 is lunar ejecta, as lunar colors are similar to those of V-type asteroids. The C and X complexes, however, can be ruled out.

We also extracted low-precision Gaia G-band photometry (Jordi et al. 2010) from our astrometric observations to derive the photometric phase curve and used it in an independent approach to constrain the spectral classification. The observations of 2020 CD_3 are limited to phase angles $36° < \alpha < 56°$ so that the back-scattering region is not covered at all. The poor phase-curve coverage does not allow for the photometric data to be fit with the standard (H_V, G_1, G_2) system in linear brightness space (Muinonen et al. 2010). Instead, we resort to the alternative technique of fitting for (H_V, G_{12}) in nonlinear magnitude space (Penttilä et al. 2016), where G_{12} is forced to stay nonnegative and, thus, physically meaningful. The nominal solution, after converting G_{12} to (G_1, G_2) and G band to V band assuming $V - G = 0.2$, is $(H_V, G_1, G_2) = (31.88^{+0.03}_{-0.05}, 0.0^{+0.10}_{-0.0}, 0.535^{+0.0}_{-0.069})$ (Figure 2(b)). We note that the formal uncertainty estimate for G_{12} is meaningless because its nominal value is a result of forcing it to be nonnegative and the above uncertainty estimates have been obtained by bootstrapping.

Assuming characteristic slope parameters (G_1, G_2) for different asteroid taxonomic types (Shevchenko et al. 2016) and fitting only for H_V, we find better fits when using slope parameters typical for E, S, and M types than for P, C, and D types (Figure 2(b) and Table 5). Fixing the slope parameters and fitting only for H_V results in lower values for the Bayesian Information Criterion than fitting for both H_V and G_{12}, suggesting that the amount of data is not necessarily sufficient for a meaningful H_V, G_{12} fit let alone a full H_V, G_1, G_2 fit. The fit is also consistent with slope parameters typical for asteroid (4) Vesta (Gehrels 1967; Shevchenko et al. 2016), the most prominent member of V-type asteroids. These results are in excellent agreement with the photometric colors.

In an alternative, synoptic, approach when fitting the radial component A_1 to photometry, the fit to the photometric phase curve results in an absolute magnitude $H_V = 31.9 \pm 0.8$ for 2020 CD_3. The value is consistent with a purely photometric

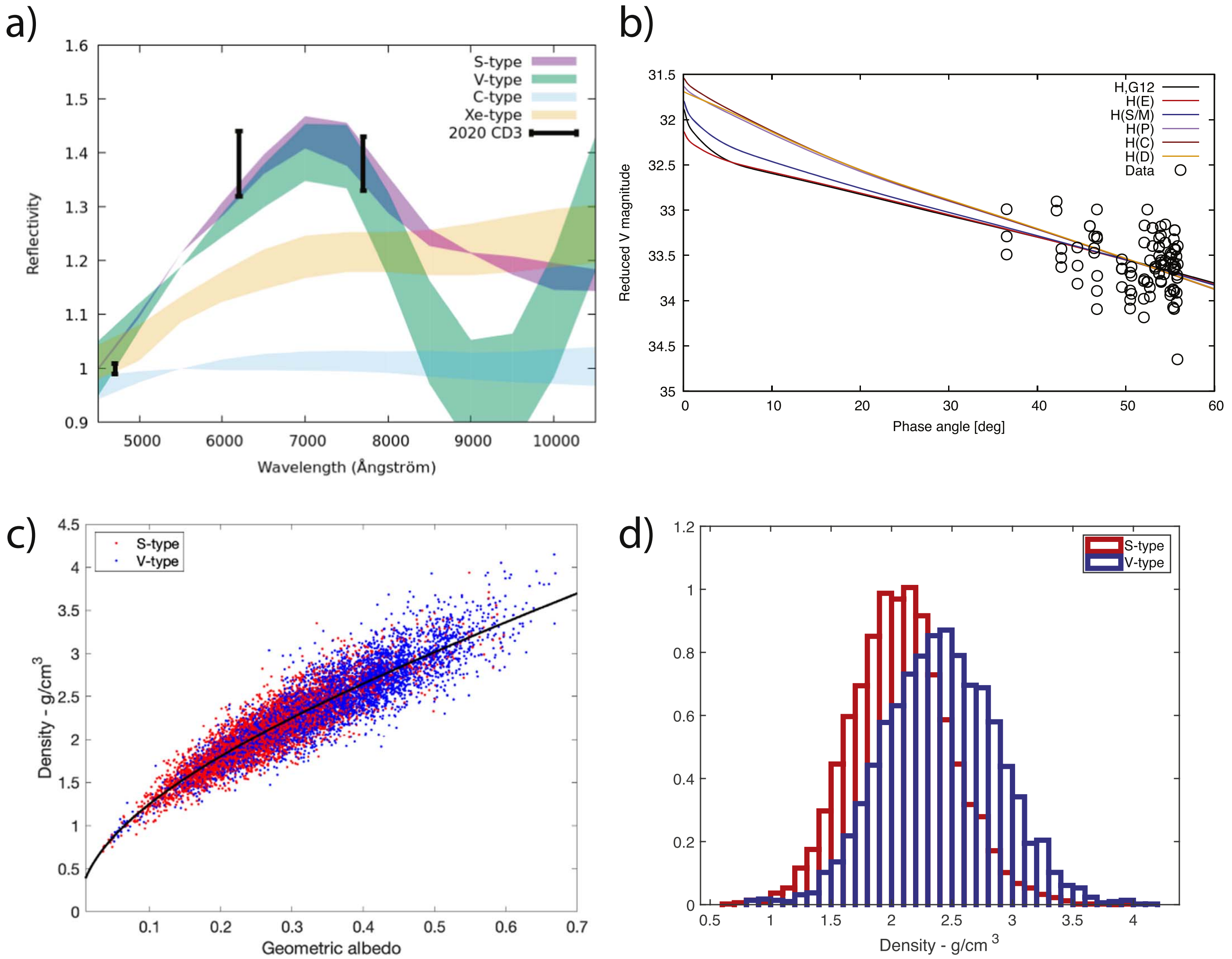

Figure 2. Physical characterization of 2020 CD$_3$. (a) Comparison of the color indices of 2020 CD$_3$ obtained with GMOS/Gemini North (black) to the reflectance spectra of the main asteroid taxonomic complexes (DeMeo et al. 2009). Spectral types C (azure) and Xe (nude, the reddest member of the X complex) can be ruled out, leaving types S (violet) and V (turquoise) as plausible choices. (b) Photometric phase curve and constrained photometric fits for 2020 CD$_3$. H, G_{12} is the nonlinear constrained two-parameter fit, and $H(\ldots)$ refer to one-parameter fits where the slope parameters have been fixed to typical values for different spectral types (E,S/M,P, C,D). (c) Scatter plot of albedo and bulk density. Red and blue dots correspond to our Monte Carlo distributions for the S and V taxonomic classes, respectively. The black curve corresponds to the best fit to the density as a function of the albedo. (d) Monte Carlo distribution of the density of 2020 CD$_3$ for the S (red) and V (blue) taxonomic classes.

Table 5
Fits of the H, G_1, G_2 System to the Photometric Phase Curve of 2020 CD$_3$

Fit Type	H_V	G_1	G_2	wRMS	ΔBIC
H(E)	32.13	0.1505	0.6005	1.632	0.000
H(S/M)	31.79	0.2588	0.3721	1.635	0.4107
H(P)	31.63	0.8343	0.04887	1.658	3.310
H(C)	31.54	0.8228	0.01938	1.661	3.686
H(D)	31.69	0.9617	0.01645	1.661	3.763
H, G_{12}	31.88	0.000	0.5324	1.630	4.418

Note. The first five fits assume values for the G_1 and G_2 parameters typical for the spectral types mentioned in the parentheses and fit for H only. The last fit allows for both H and G_{12} parameters to be fitted, but requires $0 < G_{12} < 1$, which is a physically meaningful range. The last two columns provide the weighted r s (wRMS) value and the Bayesian Information Criterion with respect to its lowest value (ΔBIC). These results have been computed with the online calculator available at http://h152.it.helsinki.fi/HG1G2/.

fit, but the error estimates are more conservative. Assuming the distribution of possible values of the geometric albedo ($p_V = 0.26 \pm 0.08$ for S types, and 0.34 ± 0.11 for V types; Mainzer et al. 2012) and the phase-curve fit for the H magnitude for S- or V-class asteroids, we obtain a diameter of $1.2^{+0.4}_{-0.2}$ m, 1 of the 10 smallest NEOs ever found as of 2020 August 10, and among the best characterized with colors, rotation period, and AMR. The derived size is consistent with the nondetection of 2020 CD$_3$ by the Arecibo radar assuming a nonmetallic material composition, excluding an artificial body or an M-type asteroid (P. Taylor 2020, personal communication).

Thus, all our evidence suggests that 2020 CD$_3$ is of spectral type S or V. Although little is known of the color distribution of meter-class asteroids, our result is consistent with the observed taxonomic distribution of NEOs with diameters <200 m where S-class objects dominate (Binzel et al. 2019).

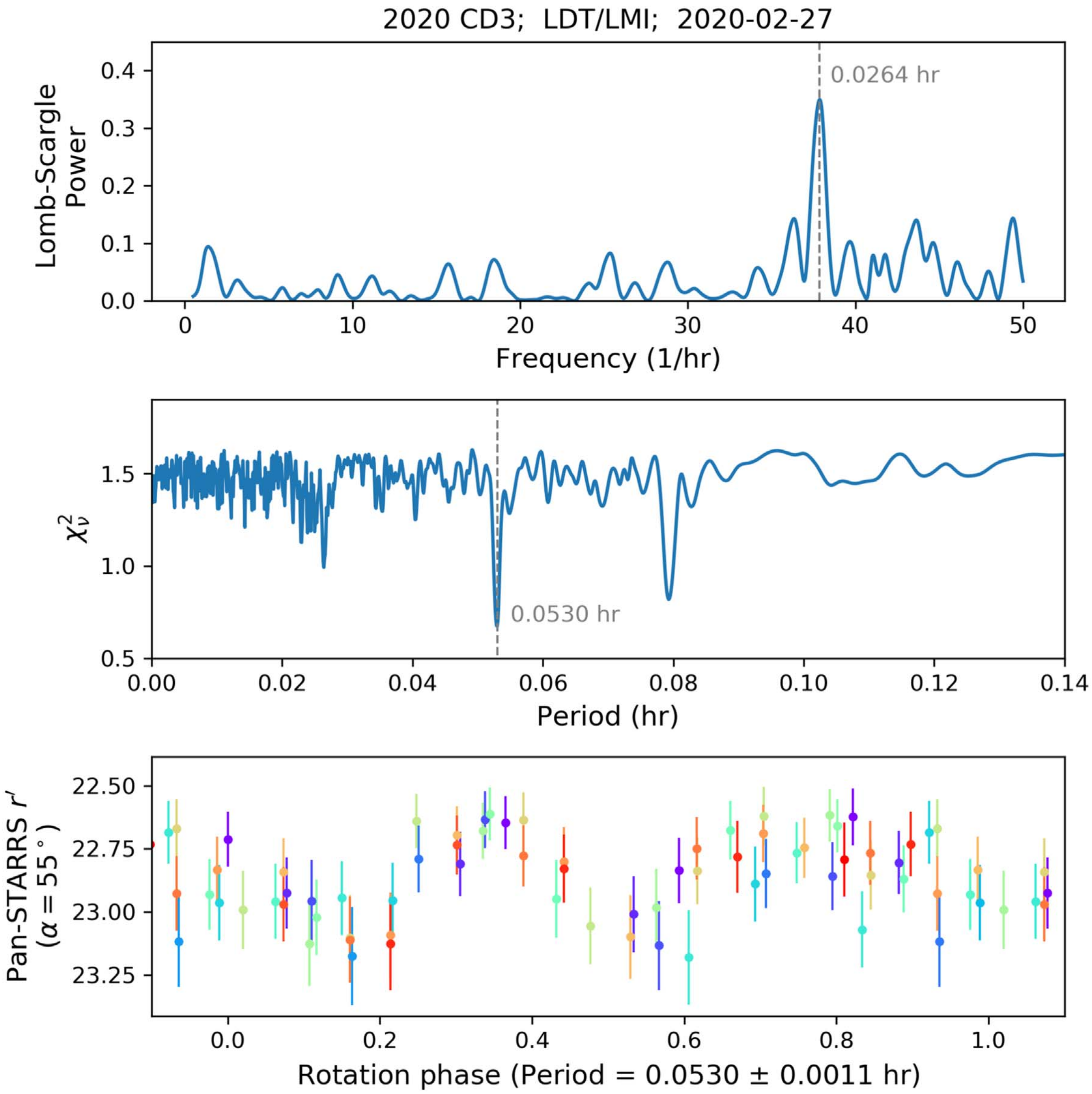

Figure 3. Lightcurve of 2020 CD_3. Top panel: the Lomb–Scargle periodogram for the rotation period of 2020 CD_3. With 30 s exposures taken over a span of 60 minutes, the range of periodogram frequencies is limited from 70 s to 2 hr. The peak in the periodogram is at 0.0264 hr. Middle panel: reduced χ^2 residuals from lightcurve curve fits using a third-order Fourier series. The best fit at 0.0530 hr corresponds to the full rotational period. Bottom panel: LDT lightcurve photometry of 2020 CD_3 calibrated to the Pan-STARRS r_{P1} filter. The 1 hr sequence of data has been phase-folded to the best-fit period of 0.0530 hr (3.2 minutes). The color scale represents the ordering of the measurements from the beginning of the sequence in blue to the end in red.

Furthermore, it is consistent with extrapolations of the asteroid taxonomic and orbital element distribution to small NEOs on Earth-like orbits, the minimoon source population, which suggest that for $H \sim 24.5$, corresponding to S-type asteroids of ∼40 m diameter, S types make up about 40% of the population (Jedicke et al. 2018b).

The lightcurve of 2020 CD_3, despite its relatively low S/N, shows a strong peak at 0.026 hr in a Lomb–Scargle periodogram and a clear minimum in χ^2 residuals from Fourier fits to the data at a period = 0.0530 hr (Figure 3). These reduced χ^2 residuals (normalized by the degrees of freedom) were computed for third-order Fourier fits across a range of periods from 0.0001 to 2 hr at a step size of 0.0001 hr. Second- and fourth-order Fourier series produced overall higher χ^2 values. An approximate 1σ error on the period of 0.0011 hr was estimated as the FWHM of the deepest minimum in the χ^2 plot. Phasing the data to periods at the limits of this uncertainty range resulted in clear decoherence of the periodic signal. The best-fit period 0.0530 ± 0.0011 hr is consistent with the Lomb–Scargle periodogram. In particular, given the apparent ∼0.5 mag peak-to-peak amplitude, the second-order harmonic ($P = 0.053$ hr) is the most probable interpretation of the Lomb–Scargle peak for data obtained at a phase angle of 55° (Butkiewicz-Bąk et al. 2017). We note that the best-fit rotational period is shorter than the individual integration times of the color photometry. Therefore, the brightness variation due to the rotation of 2020 CD_3 is averaged out in individual photometric color measurements. Assuming a double-peaked lightcurve, a period of about 3.2 minutes (∼190 s) is a reasonable interpretation; however, due to the low S/N of these data, the period is not strongly constrained. Nonprincipal axis rotation cannot be ruled out with the available data. The observed rotational period is at least an order of magnitude slower than the predicted mean value from a Maxwellian rotational distribution for meter-sized objects (Bolin et al. 2014). This implies that radar may be better suited for the detection of minimoons than had been previously anticipated, because the radar signal is smeared less by asteroid rotation than suggested by extrapolations of size–rotation-rate models.

The two unknowns in Equation (1) are the albedo and density, but they are constrained by the other measured parameters. Given that our photometric model implies that 2020 CD_3 is either an S- or V-type asteroid, we generated synthetic albedos for 10,000 of each type according to the type-specific albedo distributions of Mainzer et al. (2012). Similarly, we generated the same number of random A_1 values using a normal distribution with a mean and width given by the central value and uncertainty on our measured $A_1 = (3.1 \pm 0.2) \times 10^{-9}$ m s^{-2}. The pairs of synthetic albedo A_1 values were then used to calculate the object's density (Figures 2(c)–(d)). For the S-type assumption, we find $\rho = 2.1 \pm 0.4$ g cm^{-3} whereas for the V-type assumption, $\rho = 2.4 \pm 0.5$ g cm^{-3}. In both cases, the inferred density is consistent with typical asteroid densities (Carry 2012). We note that the possible effect of the Yarkovsky force can potentially increase the estimated density values by 10%–20% (Chesley et al. 2014) so that our density estimates represent the lower bound of values. However, this does not have a major impact on the interpretation of the results.

Thus, our physical characterization of 2020 CD_3 indicates that it is a silicate body, perhaps a free-floating analog of what appear to be monolithic boulders found on the surface of larger asteroids such as (25143) Itokawa, the S-type asteroid investigated in situ by the Hayabusa spacecraft (Saito et al. 2006). Alternatively, it could be a small rubble-pile aggregate more like 2008 TC_3 (e.g., Jenniskens et al. 2009). While the internal structure of meter-scale asteroids is currently unknown, we expect that favorable appearances of small NEOs and future minimoons will provide more opportunities for detailed characterization of these small asteroids.

4.2. Orbital Evolution

Integrating 2020 CD_3's trajectory into the past indicates that it was bound to Earth and its orbit was deterministic after a close approach to the Moon on 2017 September 15 (Figure 4(a)). Prior to this encounter, there are three possible behaviors: (1) 97.3% escape the Earth–Moon system, corresponding to a scenario in which this encounter is responsible for the capture of 2020 CD_3 by the Earth–Moon system; (2) 1.4% intersect the Moon's surface, which corresponds to the hypothesis that 2020 CD_3 is lunar ejecta; and (3) 1.3% remain in Earth orbit (potentially for more than 10 yr). Therefore, we conclude that 2020 CD_3 was in orbit around Earth since at least 2017 September 15. Since then, it completed 11 orbits around the Earth with intervals between successive perigees of 70–90 days. Its minimum geocentric distance was between 12,900 and 13,400 km on 2019 April 4, and it escaped Earth's Hill sphere (~0.01 au) on 2020 March 7 after a final perigee on 2020 February 13 at a geocentric distance of about 47,000 km. Oddly, it passed its last perigee just two days before its discovery. 2020 CD_3's Earth-like orbit means it has a long synodic orbital period so it will not approach Earth again until 2044 March at about 10 lunar distances, well outside Earth's Hill sphere.

The capture duration of 2020 CD_3 of at least 2.7 yr (Figure 4(b)) may seem exceptionally long considering that orbital simulations suggest that the average capture duration of minimoons is about nine months (Fedorets et al. 2017). However, there is an inverse correlation between the average capture duration and the minimum lunacentric distance when the encounter distance is less than 30,000 km (Figure 4(c)). In such cases, minimoons may become captured over years or even decades. Although only ~2% of minimoons have capture durations greater than three years, those objects' total capture duration time is 23% of the cumulative capture duration time of all simulated minimoons. Based on the close encounter of 2020 CD_3 with the Moon, it is not surprising that 2020 CD_3 undergoes a longer geocentric capture than an average minimoon. The distribution of possible capture durations of 2020 CD_3 is thus in agreement with theoretical predictions (Figure 4(b)).

We argue that a lunar origin for 2020 CD_3 is highly unlikely (see Section 4.3) and therefore assume that the object originated in the main asteroid belt. Based on its precapture heliocentric orbit, it has a (72 ± 1)% probability of having been ejected by the ν_6 secular resonance with, primarily, Saturn (Granvik et al. 2018). A provenance in the inner main belt would also favor its identification in the S-type taxonomy because S types dominate that region of the belt. There is a (28 ± 1)% probability for it having originated in the Hungaria region and a negligible (0.5 ± 0.03)% probability that it was ejected from the outer region of the main belt by the 3:1 mean-motion resonance with Jupiter. The reported uncertainties on the probabilities are the standard error on the mean across several discrete cells in the Granvik et al. (2018) NEO population model. An inner belt source for 2020 CD_3 is in agreement with a silicate-rich asteroid composition, which is dominant in that region (DeMeo & Carry 2014).

4.3. Exploring the Lunar Ejecta Hypothesis

There is a possibility that 2020 CD_3 could have been spall ejected by a recent lunar impact event (Section 4.2), and we assess the likelihood of this scenario by examining the contemporary production rate of small craters on the Moon.

The largest crater to form annually on the Moon is approximately 50 m in diameter based on a survey of fresh impact craters identified on the Moon using "before" and "after" images from the Lunar Reconnaissance Orbiter (LRO) Narrow Angle Camera (NAC; Speyerer et al. 2016). Accordingly, if 2020 CD_3 was launched from the lunar surface on 2017 September 15, a crater of this scale would need to be capable of launching a meter-sized minimoon off the Moon and onto the trajectory described above.

An asteroid striking the Moon creates a crater approximately 20 times its own size (Melosh 1989) so a 2.5 m diameter projectile can make a 50 m diameter crater. Hirase et al. (2004) investigated the relationship of ejecta velocity relative to the ejecta-to-impactor diameter ratio in laboratory experiments, an analysis of secondary craters produced by lunar and Martian craters, and ejecta from the asteroid (4) Vesta that make up the Vesta family (often called Vestoids). At an ejecta/impactor diameter ratio of ~0.4, corresponding to the ejection of a 1 m diameter minimoon by a 2.5 m diameter projectile, the typical ejection speeds are a few tens of m s^{-1} and certainly <100 m s^{-1}—much smaller than the lunar escape velocity (~2400 m s^{-1}). Indeed, the results of Hirase et al. (2004) analysis suggest that launching a 1 m diameter minimoon off the lunar surface requires the impact of a kilometer-scale asteroid, an

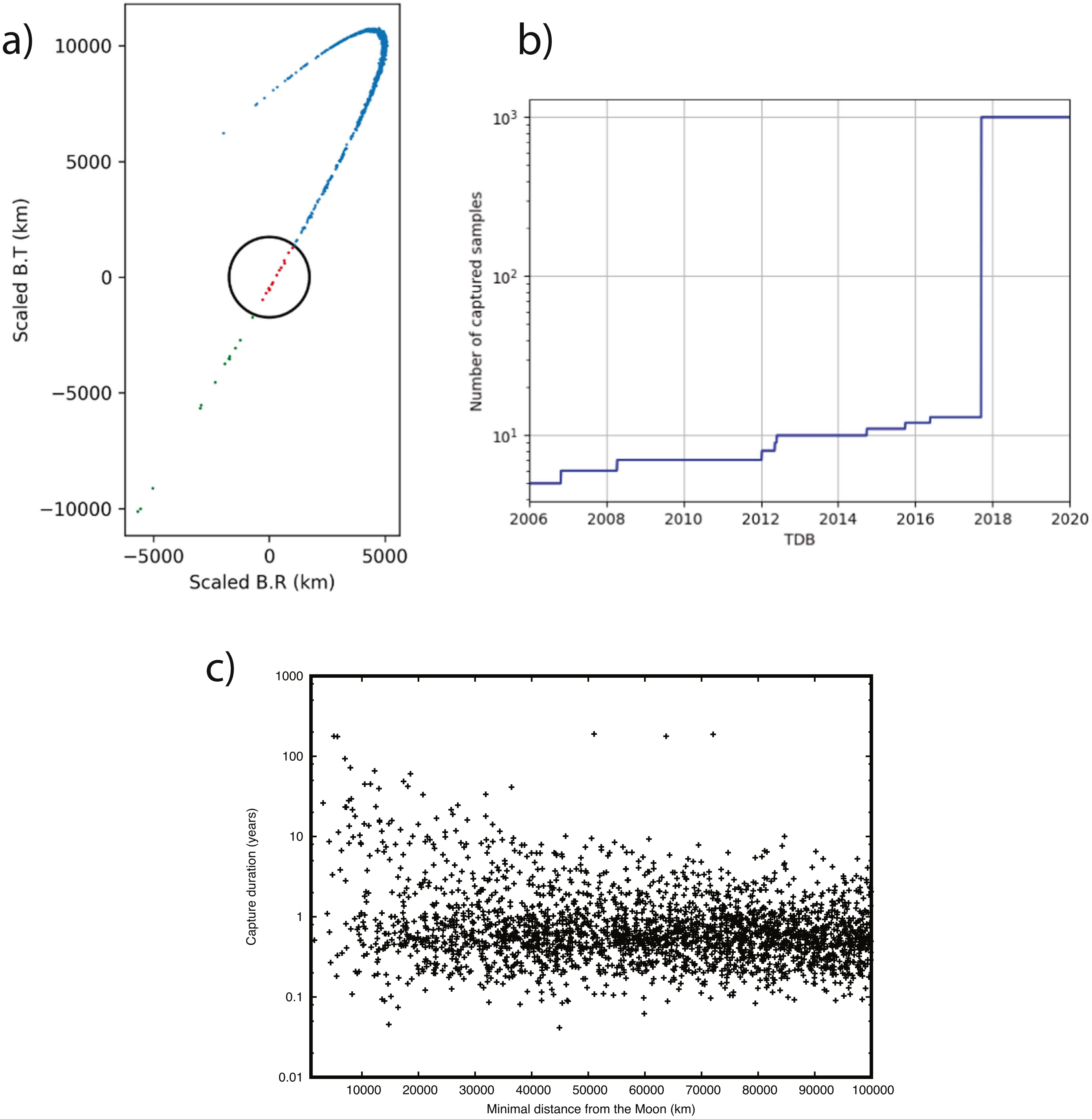

Figure 4. Orbital evolution of 2020 CD_3. (a) Monte Carlo samples of the 2020 CD_3 trajectory mapped onto the outbound scaled B plane (Farnocchia et al. 2019) of the Moon (black circle) on 2017 September 15. On that date, there was a close encounter between 2020 CD_3 and the Moon, which results in a trivergence of orbital solutions when going further back in time: (blue) samples captured on a geocentric orbit during this encounter, (red) samples originating from the Moon, and (green) samples remaining in an orbit around Earth prior to the encounter. (b) The cumulative number of Monte Carlo samples bound to the Earth–Moon system as a function of time when integrating backwards from 2020. (c) The capture duration of minimoons as a function of their minimum lunacentric distance (using data from Fedorets et al. 2017). A close encounter between a minimoon and the Moon typically increases the capture duration.

unlikely event that surely would have been noticed on or soon after 2017 September 15. Furthermore, the population of NEOs is $\gtrsim$90% known at this time, and no impacts were predicted on that date. Accordingly, we reject a lunar ejecta origin for 2020 CD_3. In summary, while NEO-based models (Granvik et al. 2012; Fedorets et al. 2017) indicate that an annual capture of a meter-sized asteroid is likely, the production of similar-sized lunar ejecta at the same rate can be ruled out. Hence, minimoon capture from the NEO population is a dominating mechanism for maintaining the minimoon steady-state population.

An additional blow to the lunar origin hypothesis for 2020 CD_3 comes from lunar meteorites that were blasted off the Moon in the past. Warren (1994), whose analysis builds on

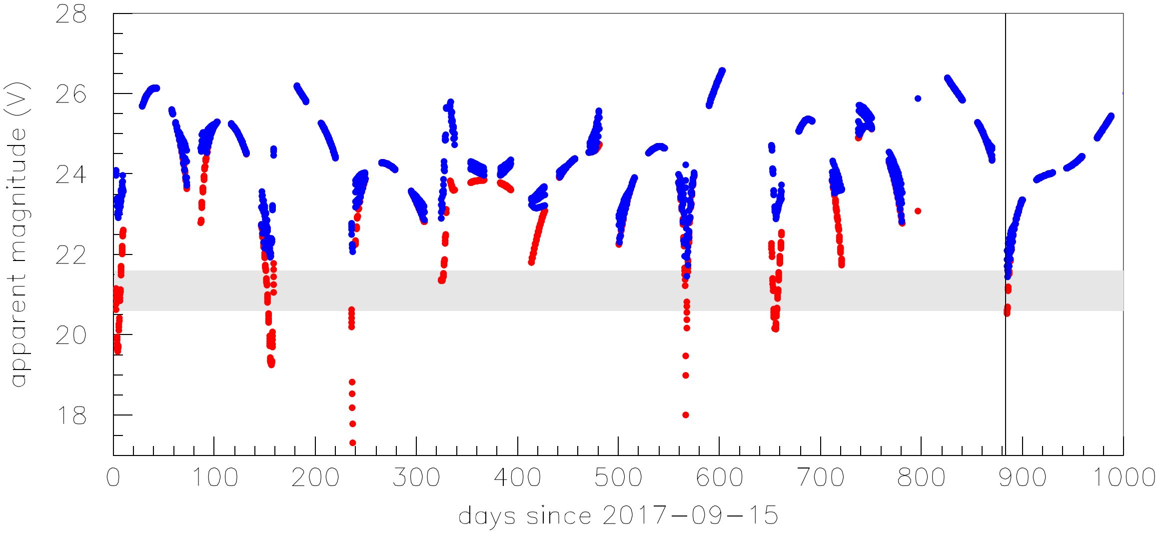

Figure 5. Detectability windows for 2020 CD_3. The red points represent 2020 CD_3's V-band apparent magnitude every 2 hr over a period of about 2.7 yr beginning on the date of its close approach to the Moon on 2017 September 15. The blue points represent 2020 CD_3's V-band apparent magnitude after accounting for trailing losses specific to the discovery observatory. To mimic CSS's observing strategy, the points are only shown when 2020 CD_3 is more than 60° from the Sun, more than 45° from the Moon when it is <50% illuminated, and from 4 to 12 hr UTC. The vertical line is on the date on which 2020 CD_3 was discovered (2020 February 15). The horizontal gray band represents ±0.5 mag centered on the average limiting magnitude of the CSS Mt. Lemmon telescope. Thus, the only time when that telescope could detect 2020 CD_3 is when blue dots appear in or below the gray band.

the work of Melosh (1985), argues that most lunar meteorites came from lunar craters that were hundreds of meters to several kilometers in diameter and that the meteoroid precursor bodies to the meteorites were 2–10 cm in diameter prior to entering Earth's atmosphere. Lunar meteorite cosmic-ray exposure ages indicate that only about half took less than 100,000 yr to get to Earth (Warren 1994). Given that minimoon orbital lifetimes are typically on the order of a year, it implies that those meteoroids spent most of their time on heliocentric orbits before being delivered back to Earth, not in the Earth–Moon system. Taken together, it suggests that it is difficult for small craters to launch sizable bodies off the Moon; if small impact events could do so, we might expect very young lunar meteorites to dominate the fall and find record on Earth.

We emphasize that the impact capable of producing an ejecta of the size of 2020 CD_3 would have been very bright. Moreover, the distribution of the subset of sample orbits originating from the Moon point the majority of them to the part of the dark size of the Moon facing toward Earth, providing optimal observing conditions (see the Appendix). No major impacts have been reported, including the NELIOTA telescope (Xilouris et al. 2018), the NASA lunar impact monitoring (W. Cooke 2020, private communication). Moreover, no reports of new kilometer-sized craters on the Moon have been announced.

In summary, we consider the lunar origin of 2020 CD_3 to be extremely unlikely.

4.4. Detectability of 2020 CD_3

The discovery of 2020 CD_3 occurred at the last window of opportunity (Figure 5). However, simulations by Fedorets et al. (2020), and the fact that 2006 RH_{120} was discovered only three months into its captured time period of one year, suggest that the last-minute discovery of 2020 CD_3 is not a typical situation. During the undisputed capture period of 2.7 yr, there were six distinct intervals during which 2020 CD_3 was brighter than the discovery observatory's (CSS's Mt. Lemmon) limiting magnitude (Figure 5). It even briefly reached $V < 16$ when it approached to within about 20,000 km, below the orbits of geosynchronous satellites. The problem is that during the detectability windows, when it was bright and close to Earth, it also had a high apparent rate of motion so that it would have left a trailed image on the detector, spreading out the light from the object and reducing the per-pixel S/N to a level below the system's detection threshold. Taking these trailing losses into account, there were only three 2 hr time segments during the entire 2.7 yr in which 2020 CD_3 was detectable by the Mt. Lemmon telescope, corresponding to ~0.03% of the time under the best of circumstances. A similar analysis for the Pan-STARRS1 telescope (Chambers et al. 2016) finds that there were only four short time periods during which it could have detected 2020 CD_3. Pan-STARRS1 reaches a fainter limiting magnitude than Mt. Lemmon due to its larger aperture and better seeing statistics, but its smaller pixels makes it less sensitive to fast-moving objects like minimoons.

4.5. Minimoon Population

We expect there to exist a much larger but undiscovered population of minimoons that are similar or smaller in size than 2020 CD_3 (Fedorets et al. 2017; Granvik et al. 2012)—they are just difficult to detect due to their faintness, rate of motion, and infrequent windows of observational opportunity (Figure 5). Estimating the minimoon population's size–frequency distribution by debiasing the discovered population of two objects is essentially impossible given that they are so difficult to detect and were at the limit of the system's detection capability. In addition to the two minimoons discovered by CSS, observations of meteors created by meteoroids that had a high probability of being geocentric prior to entering the atmosphere (Clark et al. 2016; Shober et al. 2019) support the existence of a minimoon population. These meteor observations are also difficult to convert into a minimoon population estimate because a meteor's apparent brightness, in both the optical and radar, is dominated by the meteoroids diameter and its speed. Because meteors generated by minimoons have the lowest possible meteor speed, essentially equal to Earth's escape speed, they are the faintest possible meteors. Thus, in order for them to be bright enough to be detected, they must be large and therefore rare.

To quantify the detection frequency of minimoons, we apply Bolin et al.'s (2014) modeling of the performance of Pan-STARRS1 survey (PS1; Chambers et al. 2016) to the CSS's Mt. Lemmon observatory that discovered both of the telescopically identified minimoons. The application is appropriate because the two observatories have roughly similar capabilities, especially considering all the difficulties involved in modeling the detection of faint, fast-moving minimoons, and the statistics of just two objects. The modeled PS1 survey has a peak probability of detecting minimoons at $H_V = 31.5 \pm 1.5$ so Mt. Lemmon's discovery of 2020 CD_3 with $H_V = 31.9 \pm 0.8$ is not surprising. Furthermore, Bolin et al. (2014) estimated that PS1 (and therefore Mt. Lemmon) could detect about 0.01 minimoons per lunation or about one every ~8.1 yr as compared to the ~14 yr interval since CSS's discovery of 2006 RH_{120}. We think the ~2× discrepancy in the time interval is not significant given that (1) Bolin et al. (2014) used the earlier and larger minimoon size–frequency distribution of Granvik et al. (2012) compared to the revised distribution of Fedorets et al. (2017) and because (2) it is intrinsically difficult to model discovery rates at the limits of detectability in both flux and rate of motion (see Figure 5). Moreover, assuming Poisson-like discovery statistics and that the CSS Mt. Lemmon survey has been in operation at roughly the same capability level for 20 yr, over the same period, there is a ~68% probability of discovering $\leqslant 2$ minimoons. Therefore, the discovery of 2020 CD_3 14 yr after the discovery of 2006 RH_{120}, a minimoon with $H_V = 29.9 \pm 0.3$, is in line with the capture frequency of minimoons predicted by existing population models and consistent with their predicted discovery rate (Bolin et al. 2014).

An additional complication in debiasing the minimoon population identified in asteroid surveys is the difficulty of identifying rare natural objects among numerous artificial ones (Jedicke et al. 2018a). As sky surveys have become more powerful and efficient at identifying faint and trailed objects, they have been detecting ever more artificial geocentric objects, often on minimoon-like orbits. Distinguishing both 2020 CD_3 and 2006 RH_{120} from artificial objects upon their discovery was initially inadvertently affected by human biases that objects on geocentric orbits are artificial and correcting the observation statistics for this bias will be difficult.

5. Conclusions

We provide an in-depth study of the orbital and physical characteristics of Earth's second discovered minimoon, 2020 CD_3. The combination of its area-to-mass ratio derived from its solar radiation pressure signature, its reflectance spectrum that is consistent with silicate asteroids, and its nondetection by radar provides evidence that 2020 CD_3 is a natural object. Its derived geometric albedo—bulk density distributions are consistent with values typical of silicate asteroids. 2020 CD_3 could be a free-floating silicate analog of boulders discovered on surfaces of larger asteroids.

High-precision astrometry enabled by the Gaia mission permits the measurement of ground-based astrometry of asteroids to a level of $0\overset{''}{.}05$ in the best cases. This, in turn, provides better, faster constraints on the solar radiation pressure signature for small asteroids. For the best possible results, special attention needs to be paid to (1) using accurate and precise geographical coordinates for ground-based observatories and (2) time-keeping.

The geocentric orbital evolution of 2020 CD_3 includes a close dynamical interaction with the Moon on 2017 September 15. It was bound on a geocentric orbit for at least 2.7 yr, which makes it an exceptionally long capture compared to typical capture duration results from simulations. However, a long duration is actually typical for minimoons that experience close approaches to the Moon. Some orbital trajectories suggest a lunar ejecta origin of 2020 CD_3, but we showed that this possibility is unlikely.

The discovery of 2020 CD_3 is in line with the most recent theoretical predictions for the steady-state population of minimoons (Fedorets et al. 2017), supporting the prediction for an increased discovery rate of minimoons (Fedorets et al. 2020) with the upcoming Vera C. Rubin Observatory's Legacy Survey of Space and Time (LSST; Ivezić et al. 2019). More discoveries of minimoons are also anticipated through improvements to the ongoing NEO surveys such as CSS (Bolin et al. 2014), but trailing losses remain a major factor affecting the discovery of minimoons. A rapid determination of the nature of temporarily captured objects after their discovery remains a challenge that is expected to become even more pressing with the anticipated increase in their discovery rate with LSST.

The discovery and characterization of 2020 CD_3 paves the way for the observational study of minimoons as a population instead of a curiosity with serendipitous discoveries, as well as for identifying candidate targets for cost-effective space missions to these unexplored objects at the asteroid–meteoroid boundary (Granvik et al. 2013; Jedicke et al. 2018a).

The authors thank Bryce Bolin, William Cooke, Alan Fitzsimmons, Tomáš Kohout, Antti Penttilä, Patrick Taylor, and Anne Virkki for helpful discussions, the anonymous referee for insightful comments, and Daniel Hestroffer for his hospitality during the research visit of G.F. to the Paris Observatory.

Based on observations made with the Nordic Optical Telescope, operated by the Nordic Optical Telescope Scientific Association at the Observatorio del Roque de los Muchachos, La Palma, Spain, of the Instituto de Astrofisica de Canarias. The data presented here were obtained in part with ALFOSC, which is provided by the Instituto de Astrofisica de Andalucia (IAA) under a joint agreement with the University of Copenhagen and NOTSA.

Based on observations obtained with MegaPrime/MegaCam, a joint project of CFHT and CEA/DAPNIA, at the Canada–France–Hawaii Telescope (CFHT) which is operated by the National Research Council (NRC) of Canada, the Institut National des Sciences de l'Univers of the Centre National de la Recherche Scientifique (CNRS) of France, and the University of Hawaii. The observations at the CFHT were performed with care and respect from the summit of Maunakea, which is a significant cultural and historic site.

The authors acknowledge the sacred nature of Maunakea and appreciate the opportunity to obtain observations from the mountain. This work is partly based on observations obtained at the international Gemini Observatory, a program of NSF's OIR Lab, which is managed by the Association of Universities for Research in Astronomy (AURA) under a cooperative agreement with the National Science Foundation. On behalf of the Gemini Observatory partnership: the National Science Foundation (United

States), National Research Council (Canada), Agencia Nacional de Investigación y Desarrollo (Chile), Ministerio de Ciencia, Tecnología e Innovación (Argentina), Ministério da Ciência, Tecnologia, Inovações e Comunicações (Brazil), and Korea Astronomy and Space Science Institute (Republic of Korea). The observations were obtained as part of Gemini Director's Discretionary Program GN-2020A-DD-107. The GMOS-N observations were acquired through the Gemini Observatory Archive at NSF's NOIRLab and processed using DRAGONS (Data Reduction for Astronomy from Gemini Observatory North and South).

This work was enabled by observations obtained with the University of Hawai'i's 2.2 m telescope and the Gemini North telescope, and the Canada–France–Hawaii telescope, all located within the Maunakea Science Reserve and adjacent to the summit of Maunakea. We are grateful for the privilege of observing the Universe from a place that is unique in both its astronomical quality and its cultural significance.

These results made use of the 4.3 m Lowell Discovery Telescope at Lowell Observatory. Lowell is a private, nonprofit institution dedicated to astrophysical research and public appreciation of astronomy and operates the LDT in partnership with Boston University, the University of Maryland, the University of Toledo, Northern Arizona University, and Yale University. The Large Monolithic Imager was built by Lowell Observatory using funds provided by the National Science Foundation (AST-1005313). Part of the LDT observations have been obtained thanks to the NASA SSO-NEOO grant No. 80NSSC19K1586. Some of the LDT observations were obtained by the University of Maryland observing team, consisting of L. M. Feaga, Q.-Z. Ye, J. M. Bauer, T. L. Farnham, C. E. Holt, M. S. P. Kelley, J. M. Sunshine, and M. M. Knight.

This work has made use of data from the European Space Agency (ESA) mission Gaia (https://www.cosmos.esa.int/gaia), processed by the Gaia Data Processing and Analysis Consortium (DPAC, https://www.cosmos.esa.int/web/gaia/dpac/consortium). Funding for the DPAC has been provided by national institutions, in particular the institutions participating in the Gaia Multilateral Agreement.

Based on the observations obtained with the Chinese Near-Earth Object Survey Telescope (CNEOST). We thank Bin Li for providing the exposure catalog.

Based on observations obtained with the Samuel Oschin 48 inch Telescope at the Palomar Observatory as part of the Zwicky Transient Facility project. ZTF is supported by the National Science Foundation under grant No. AST-1440341 and a collaboration including Caltech, IPAC, the Weizmann Institute for Science, the Oskar Klein Center at Stockholm University, the University of Maryland, the University of Washington, Deutsches Elektronen-Synchrotron and Humboldt University, Los Alamos National Laboratories, the TANGO Consortium of Taiwan, the University of Wisconsin at Milwaukee, and Lawrence Berkeley National Laboratories. Operations are conducted by COO, IPAC, and UW.

The Catalina Sky Survey has been funded since 1998 by the National Aeronautics and Space Administration's Near Earth Object Observations program, currently under grant No. 80NSSC18K1130.

The Pan-STARRS1 Surveys (PS1) have been made possible through contributions by the Institute for Astronomy, the University of Hawaii, the Pan-STARRS Project Office, the Max Planck Society and its participating institutes, the Max Planck Institute for Astronomy, Heidelberg, and the Max Planck Institute for Extraterrestrial Physics, Garching, The Johns Hopkins University, Durham University, the University of Edinburgh, the Queen's University Belfast, the Harvard-Smithsonian Center for Astrophysics, the Las Cumbres Observatory Global Telescope Network Incorporated, the National Central University of Taiwan, the Space Telescope Science Institute, and the National Aeronautics and Space Administration under grant No. NNX08AR22G issued through the Planetary Science Division of the NASA Science Mission Directorate, the National Science Foundation grant No. AST-1238877, the University of Maryland, Eötvös Loránd University (ELTE), and the Los Alamos National Laboratory.

M.M. would like to thank Detlef Koschny, Luca Conversi, and Erwin Schwab for their support with the CAHA Schmidt observations.

G.F. was supported by STFC Grant ST/P000304/1. M.G. was partly supported by the Academy of Finland. Support for M.D. and N.M. was provided by NASA NEOO grant NNX17AH06G in support of the Mission Accessible Near-Earth Object Survey (MANOS). W.B. and R.J. were supported in part by NASA's Near Earth Object Observations program (grant No. 80NSSC17K0153). L.B. acknowledges funding from the Science Technology Funding Council (STFC) Grant Code ST/T506369/1. T.S. is supported by Gemini Observatory through a Gemini Science Fellowship. Part of this research was conducted at the Jet Propulsion Laboratory, California Institute of Technology, under a contract with NASA.

G.F., M.M., R.J., S.N, D.Fa., M.G., N.M., M.S., R.We., K. W., E.C., Q.Y., and W.B. wrote the paper. K.W. and T.P. discovered the object. G.F and M.M. acquired the NOT data, supported by A.D. R.We. and R.Wa. acquired the CFHT data. N.M., Q.Y., M.D., and M.M. acquired the LDT data. D.Fö. acquired the UH88 data. G.F., M.S., L.B., M.M., and M.G. wrote the Gemini North DD proposal. M.S., G.F., T.S., D.M. F., J.R., and A.S. acquired the Gemini North data. M.M., R. We., and Q.Y. searched for precovery images. M.M. and D.Fa. computed the area-to-mass ratio. N.M. derived the rotational period. D.Fa., M.M., M.G., R.J., and G.F. physically characterized the object. S.N., D.Fa., and M.M. calculated the orbit. W.B. and R.J. investigated the lunar ejecta hypothesis. M.G. estimated the source region of the object. R.J., E.C., R. We., and M.M. investigated the detectability of the object. R.J., G.F., M.M., M.G., and D.Fa. interpreted the results.

This work made use of NASA's Astrophysics Data System Bibliographic Services and the data and services provided by the International Astronomical Union's Minor Planet Center. (https://minorplanetcenter.net/data).

Software: DAOPHOT (Stetson 1987), IRAF (Tody 1986, 1993), NASA NAIF SPICE tools (Acton 1996; Acton et al. 2018), Sextractor (Bertin & Arnouts 1996), DRAGONS (AURA Gemini Observatory-Science User Support Department 2018), Photometry Pipeline (Mommert 2017).

Appendix

As described in Section 4.3, the lunar origin for 2020 CD_3 is extremely unlikely. We show the distribution of possible points of origin of 2020 CD_3 from the Moon for that low-probability scenario in Figure 6.

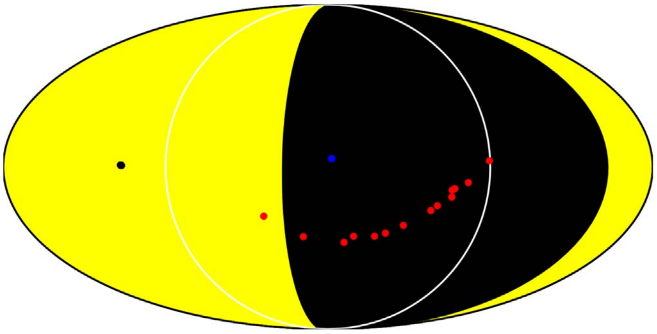

Figure 6. Mollweide projection of the surface of the Moon on 2017 September 15. Yellow and black regions show the day and night sides of the Moon, respectively. Red points show the locations from where the 2020 CD_3 samples from the lunar origin hypothesis are ejected. Blue and black points show the sub-Earth and subsolar points corresponding to the sample ejection times. White circle encloses the area of the Moon visible from Earth.

ORCID iDs

Grigori Fedorets https://orcid.org/0000-0002-8418-4809
Marco Micheli https://orcid.org/0000-0001-7895-8209
Robert Jedicke https://orcid.org/0000-0001-7830-028X
Shantanu P. Naidu https://orcid.org/0000-0003-4439-7014
Davide Farnocchia https://orcid.org/0000-0003-0774-884X
Mikael Granvik https://orcid.org/0000-0002-5624-1888
Nicholas Moskovitz https://orcid.org/0000-0001-6765-6336
Megan E. Schwamb https://orcid.org/0000-0003-4365-1455
Robert Weryk https://orcid.org/0000-0002-0439-9341
Kacper Wierzchoś https://orcid.org/0000-0002-4884-9367
William F. Bottke https://orcid.org/0000-0002-1804-7814
Quanzhi Ye https://orcid.org/0000-0002-4838-7676
Richard Wainscoat https://orcid.org/0000-0002-1341-0952
Maxime Devogèle https://orcid.org/0000-0002-6509-6360
Laura E. Buchanan https://orcid.org/0000-0002-8032-4528
Anlaug Amanda Djupvik https://orcid.org/0000-0001-6316-9880
Joel Roediger https://orcid.org/0000-0002-0363-4266
Tom Seccull https://orcid.org/0000-0001-5605-1702

References

Acton, C., Bachman, N., Semenov, B., & Wright, E. 2018, P&SS, 150, 9
Acton, C. H. 1996, P&SS, 44, 65
Alam, S., Albareti, F. D., Allende Prieto, C., et al. 2015, ApJS, 219, 12
AURA Gemini Observatory-Science User Support Department 2018, DRAGONS: Gemini Observatory Data Reduction Platform, version 2.1.0, Astrophysics Source Code Library, ascl:1811.002
Bellm, E. C., Kulkarni, S. R., Graham, M. J., et al. 2019, PASP, 131, 018002
Bertin, E., & Arnouts, S. 1996, A&AS, 117, 393
Binzel, R., DeMeo, F., Turtelboom, E., et al. 2019, Icar, 324, 41
Bolin, B., Jedicke, R., Granvik, M., et al. 2014, Icar, 241, 280
Bressi, T. H., Hergenrother, C. W., Christensen, E. J., et al. 2008, MPEC, 2008, D12
Brown, P., Spalding, R. E., ReVelle, D. O., Tagliaferri, E., & Worden, S. 2002, Natur, 420, 294
Brown, P. G., Assink, J. D., Astiz, L., et al. 2013, Natur, 503, 238
Butkiewicz-Bąk, M., Kwiatkowski, T., Bartczak, P., Dudziński, G., & Marciniak, A. 2017, MNRAS, 470, 1314
Carry, B. 2012, P&SS, 73, 98
Chambers, K. C., Magnier, E. A., Metcalfe, N., et al. 2016, arXiv:1612.05560
Chesley, S. R., Farnocchia, D., Nolan, M. C., et al. 2014, Icar, 235, 5
Christensen, E., Africano, B., Farneth, G., et al. 2018, AAS/DPS Meeting, 50, 310.10
Clark, D. L., Spurný, P., Wiegert, P., et al. 2016, AJ, 151, 135
DeMeo, F. E., Binzel, R. P., Slivan, S. M., & Bus, S. J. 2009, Icar, 202, 160
DeMeo, F. E., & Carry, B. 2013, Icar, 226, 723
DeMeo, F. E., & Carry, B. 2014, Natur, 505, 629
Farnocchia, D., Chesley, S., & Micheli, M. 2015a, Icar, 258, 18
Farnocchia, D., Chesley, S. R., & Chamberlin, A. B. 2016, AAS/DPS Meeting, 48, 305.03
Farnocchia, D., Chesley, S. R., Milani, A., Gronchi, G. F., & Chodas, P. W. 2015b, in Asteroids IV, ed. P. Michel, F. DeMeo, & W. F. Bottke (Tucson, AZ: Univ. Arizona Press), 815
Farnocchia, D., Eggl, S., Chodas, P. W., Giorgini, J. D., & Chesley, S. R. 2019, CeMDA, 131, 36
Farnocchia, D., Tholen, D. J., Micheli, M., et al. 2017, AAS/DPS Meeting, 49, 100.09
Fedorets, G., Granvik, M., & Jedicke, R. 2017, Icar, 285, 83
Fedorets, G., Granvik, M., Jones, R. L., Jurić, M., & Jedicke, R. 2020, Icar, 338, 113517
Flewelling, H. A., Magnier, E. A., Chambers, K. C., et al. 2020, ApJS, 251, 7
Fukugita, M., Ichikawa, T., Gunn, J. E., et al. 1996, AJ, 111, 1748
Gaia Collaboration, Brown, A. G. A., Vallenari, A., et al. 2018, A&A, 616, A1
Gaia Collaboration, Prusti, T., de Bruijne, J. H. J., et al. 2016, A&A, 595, A1
Gehrels, T. 1967, AJ, 72, 929
Graham, M. J., Kulkarni, S. R., Bellm, E. C., et al. 2019, PASP, 131, 078001
Granvik, M., Jedicke, R., Bolin, B., et al. 2013, in Asteroids. Prospective Energy and Material Resources, ed. V. Badescu (Berlin: Springer), 151
Granvik, M., Morbidelli, A., Jedicke, R., et al. 2016, Natur, 530, 303
Granvik, M., Morbidelli, A., Jedicke, R., et al. 2018, Icar, 312, 181
Granvik, M., Vaubaillon, J., & Jedicke, R. 2012, Icar, 218, 262
Harris, A. W., & D'Abramo, G. 2015, Icar, 257, 302
Hirase, Y., Nakamura, A. M., & Michikami, T. 2004, P&SS, 52, 1103
Hook, I. M., Jørgensen, I., Allington-Smith, J. R., et al. 2004, PASP, 116, 425
Ivezić, Ž., Kahn, S. M., Tyson, J. A., et al. 2019, ApJ, 873, 111
Jedicke, R., Bolin, B. T., Bottke, W. F., et al. 2018a, FrASS, 5, A13
Jedicke, R., Sercel, J., Gillis-Davis, J., Morenz, K. J., & Gertsch, L. 2018b, P&SS, 159, 28
Jenniskens, P., Albers, J., Koop, M. W., et al. 2016, in 54th AIAA Aerospace Sciences Meeting (Reston, VA: AIAA),
Jenniskens, P., Shaddad, M. H., Numan, D., et al. 2009, Natur, 458, 485
Jordi, C., Gebran, M., Carrasco, J. M., et al. 2010, A&A, 523, A48
Kwiatkowski, T., Kryszczyńska, A., Polińska, M., et al. 2009, A&A, 495, 967
Lindegren, L., Hernández, J., Bombrun, A., et al. 2018, A&A, 616, A2
Mainzer, A., Masiero, J., Grav, T., et al. 2012, ApJ, 745, 7
Marsden, B. 1969, AJ, 74, 720
Marsden, B., Sekanina, Z., & Yeomans, D. K. 1973, AJ, 78, 211
Masci, F. J., Laher, R. R., Rusholme, B., et al. 2019, PASP, 131, 018003
Melosh, H. J. 1985, Geo, 13, 144
Melosh, H. J. 1989, Impact Cratering: A Geologic Process (Oxford: Oxford Univ. Press)
Micheli, M., Tholen, D. J., & Elliott, G. T. 2012, NewA, 17, 446
Micheli, M., Tholen, D. J., & Elliott, G. T. 2013, Icar, 226, 251
Micheli, M., Tholen, D. J., & Elliott, G. T. 2014, ApJL, 788, L1
Miles, R. 2011, JBAA, 121, 350
Minor Planet Center 2020, MPEC, 2020, D104
Mommert, M. 2017, A&C, 18, 47
Mommert, M., Farnocchia, D., Hora, J. L., et al. 2014a, ApJL, 789, L22
Mommert, M., Hora, J. L., Farnocchia, D., et al. 2014b, ApJ, 786, 148
Muinonen, K., Belskaya, I. N., Cellino, A., et al. 2010, Icar, 209, 542
Penttilä, A., Shevchenko, V. G., Wilkman, O., & Muinonen, K. 2016, P&SS, 123, 117
Pravec, P., & Harris, A. W. 2007, Icar, 190, 250
Rabinowitz, D., Helin, E., Lawrence, K., & Pravdo, S. 2000, Natur, 403, 165
Saito, J., Miyamoto, H., Nakamura, R., et al. 2006, Sci, 312, 1341
Seidelmann, P. K., Abalakin, V. K., Bursa, M., et al. 2002, CeMDA, 82, 83
Shevchenko, V. G., Belskaya, I. N., Muinonen, K., et al. 2016, P&SS, 123, 101
Shober, P. M., Jansen-Sturgeon, T., Sansom, E. K., et al. 2019, AJ, 158, 183
Speyerer, E. J., Povilaitis, R. Z., Robinson, M. S., Thomas, P. C., & Wagner, R. W. 2016, Natur, 538, 215
Stetson, P. B. 1987, PASP, 99, 191
Tody, D. 1986, Proc. SPIE, 627, 733
Tody, D. 1993, in ASP Conf. Ser. 52, Astronomical Data Analysis Software and Systems II, ed. R. J. Hanisch, R. J. V. Brissenden, & J. Barnes (San Francisco, CA: ASP), 173
Tricarico, P. 2017, Icar, 284, 416
Vokrouhlický, D. 1998, A&A, 335, 1093
Vokrouhlický, D., & Milani, A. 2000, A&A, 362, 746
Warren, P. H. 1994, Icar, 111, 338
Xilouris, E. M., Bonanos, A. Z., Bellas-Velidis, I., et al. 2018, A&A, 619, A141
Zhao, H., Yao, J., & Lu, H. 2007, in Proc. IAU Symp. 248, A Giant Step: from Milli- to Micro-arcsecond Astrometry, ed. M. Perryman, I. Platais, & W. Jin (Cambridge: Cambridge Univ. Press), 565